Magnetoelectric materials for miniature, wireless neural stimulation at therapeutic frequencies

Amanda Wickens[1,2], Benjamin Avants[2], Nishant Verma[3], Eric Lewis[2], Joshua C. Chen[3], Ariel K. Feldman[4,5], Shayok Dutta[2], Joshua Chu[2], John O'Malley[6], Michael Beierlein[6], Caleb Kemere[2,3], Jacob T. Robinson[1,2,3,7]

[1]Applied Physics Program, Rice University, Houston, Texas, USA, [2]Department of Electrical and Computer Engineering, Rice University, Houston, Texas, USA, [3]Department of Bioengineering, Rice University, Houston, Texas, USA, [4]Department of Computer Science, Rice University, Houston, Texas, USA, [5]Department of Cognitive Science, Rice University, Houston, Texas, USA, [6]Department of Neurobiology and Anatomy, McGovern Medical School at UTHealth, Houston, Texas, USA, [7]Department of Neuroscience, Baylor College of Medicine, Houston, Texas, USA

A fundamental challenge for bioelectronics is to deliver power to miniature devices inside the body. Wires are common failure points and limit device placement. Wireless power by electromagnetic or ultrasound waves must overcome absorption by the body and impedance mismatches between air, bone, and tissue. Magnetic fields, on the other hand, suffer little absorption by the body or differences in impedance at interfaces between air, bone, and tissue. These advantages have led to magnetically-powered stimulators based on induction or magnetothermal effects. However, fundamental limitations in these power transfer technologies have prevented miniature magnetically-powered stimulators from applications in many therapies and disease models because they do not operate in clinical "high-frequency" ranges above 20 Hz. Here we show that magnetoelectric materials – applied for the first time in bioelectronics devices – enable miniature magnetically-powered neural stimulators that operate at clinically relevant high-frequencies. As an example, we show that ME neural stimulators can effectively treat the symptoms of a Parkinson's disease model in a freely behaving rodent. We also show that ME-powered devices can be miniaturized to sizes smaller than a grain of rice while maintaining effective stimulation voltages. These results suggest that ME materials are an excellent candidate for wireless power delivery that will enable miniature neural stimulators in both clinical and research applications.

Wireless neural stimulators have the potential to provide less invasive, longer lasting interfaces to brain regions and peripheral nerves compared to battery-powered devices or wired stimulators. Indeed, wires are a common failure point for bioelectronic devices. Percutaneous wires present a pathway for infection[1] and implanted wires can also limit the ability of the stimulators to move with the tissue, leading to a foreign body response or loss of contact with the target tissue[2,3]. Additionally, chronic stress and strain on wires, particularly for devices in the periphery, can lead to failure in the wire itself or its connection to the stimulator[4]. In small animals like rats and mice, wires used to power neural stimulators can interfere with natural behavior, particularly when studying social interaction between multiple animals[5].

One of the primary challenges for wireless neural stimulators is to create efficient miniature devices (< 1 cm in length) that operate reliably beneath bone and tissue as an animal or human patient engages in normal activity. At lengths of less than 1 cm, devices could be fully implanted in the periphery and be light enough to allow for unrestricted animal behavior; however for devices this small, power delivery remains a challenge. Efficient power transfer with propagating electromagnetic waves requires antennas with feature sizes comparable to the electromagnetic wavelength. Thus, for sub-millimeter devices, such as the proposed RF powered "neurograins[6]," effective power-transfer frequencies lie in the GHz range, where electromagnetic radiation is absorbed by the body[7]. Absorption of this radio-frequency electromagnetic energy limits the amount of power that can be safely delivered to implants deep inside tissue[7]. As a result, researchers typically turn to magnetic induction or batteries to power implanted devices; however, these techniques also limit the degree of miniaturization. Batteries increase the size of the device and add considerable weight. Additionally, batteries require replacement or charging, which can limit the potential uses. Inductively coupled coils, on the other hand, can be made smaller and lighter than batteries, however; the power a receiving coil can generate is directly related to the amount of flux captured by the area of the coils. Thus, when the receiver coils are miniaturized, the output power reduces and becomes more sensitive to perturbations in the distance or angle between the transmitter and receiver[8]. For example, Freeman et al. demonstrated that small inductive coils less than 1 mm in diameter can power stimulators for the sciatic nerve in anesthetized rats[9]; however, in its present form, this device would have difficulty providing stable stimulation in freely moving animals due to the reduced power coupling efficiency that accompanies changes in the angle and distance between the receiver and transmitter coils.

Additionally, for neural stimulators to treat a number of neurological disorders like Parkinson's Disease (PD), obsessive-compulsive disorder, and epilepsy, they must operate safely and effectively in the high-frequency "therapeutic band" between 100 and 200 Hz[10–12]. This type of high-frequency neural stimulation is challenging because charge on the electrode must be dissipated between successive stimulation pulses to prevent electrolysis, tissue damage, and changes to the local pH[13]. Charge dissipation at high-frequencies is accomplished by using a biphasic stimulus waveform that actively or passively charges and discharges the electrode with each cycle. Indeed all clinically approved electrical neural stimulation therapies in this therapeutic band use various forms of "charge balanced" biphasic stimulation waveforms[14].

Recently, several promising alternatives to magnetic induction and batteries have enabled miniature neural stimulators; however, these approaches have yet to demonstrate *in vivo* operation in the therapeutic high-frequency band in freely moving animals. Montgomery et al. and Ho et al. have shown that one can use the mouse body as an electromagnetic resonant cavity to effectively transfer energy to sub-wavelength scale devices implanted inside the animal[15,16]. This approach is

particularly effective to drive tiny LEDs for optogenetic stimulation. However, because the electrical waveform is monophasic, electrical stimulation has been limited to < 20 Hz. Using superparamagnetic nanoparticles to absorb energy from high-frequency (500 kHz) magnetic fields[17], one can heat specific regions of the brain [18,19] in freely moving animals[19]. This local heat can stimulate neural activity when the targeted brain region is genetically modified to respond to changes in temperature[18,19]. However this approach requires transgenesis, which adds regulatory complexity and has yet to show high-frequency operation due the requirement for the tissue to cool between stimulation intervals. Ultrasound provides a promising and efficient method to power bioelectronic implants because ultrasound wavelengths are 10^5 times smaller than electromagnetic waves at the same frequency allowing sub-millimeter-sized devices to have wavelength-scale piezoelectric antennas [20,21]. However, implementation of these "neural dust" motes can be challenging in freely moving animals because the impedance mismatch between air, bone, and tissue requires contact between soft tissue and the ultrasound transducer for efficient power transfer. As a result, there has yet to be a demonstration of ultrasound-powered neural stimulators in freely moving animals[22].

Here we show that magnetoelectric (ME) materials enable the first magnetically powered miniature neural stimulators that operate in the therapeutic high-frequency band. Similar to inductive coils, these materials transform a magnetic field to an electric field, but instead of using an implanted coil we use a material that generates a voltage via mechanical coupling between magnetostrictive and piezoelectric layers in a thin film. Namely, the magnetic field generates strain in the magnetostrictive layer as the magnetic dipoles align with the applied field. That strain exerts a force on the piezoelectric layer, which generates a voltage (Fig. 1). By exploiting this transduction mechanism, magnetoelectrics do not suffer from the same miniaturization constraints as coils and can be driven by weak magnetic fields on the order of a few millitesla. These properties have led researchers to propose magnetoelectrics as a promising material for bioelectronic implants[23–27]. Here we demonstrate the first proof-of-principle wireless neural stimulators based on ME materials in a freely behaving rodent model for Parkinson's Disease (PD), and that these materials could power miniature devices deep within the human brain.

Fabrication and characterization of ME stimulators

We fabricated proof-of-principle ME stimulators by bonding a rectangular magnetostrictive layer (Metglas) to a platinum coated piezoelectric layer, polyvinlydine fluoride (PVDF). We then encapsulated the films in a protective parylene-C layer (8-10 μm thick) (Fig. 1a, see Methods). We used PVDF layers between 28 and 110 μm, which yielded total device thicknesses between 50-150 μm. When we measured the voltage across the film, we found a dramatic voltage increase when the applied magnetic field frequency, matches an acoustic resonant frequency (Fig. 1b). Because the resonant frequency is proportional to the inverse of the film length, we can design multiple films and selectively activate them by

140 changing the stimulus frequency (Fig. S2b). Using this principle, we can use different
141 magnetic field frequencies to activate separate devices that may be in different areas
142 of the body, or create biphasic stimulators by interleaved resonant stimulation of
143 two different films, with each film driving either the positive or negative phase of
144 the neural stimulus.

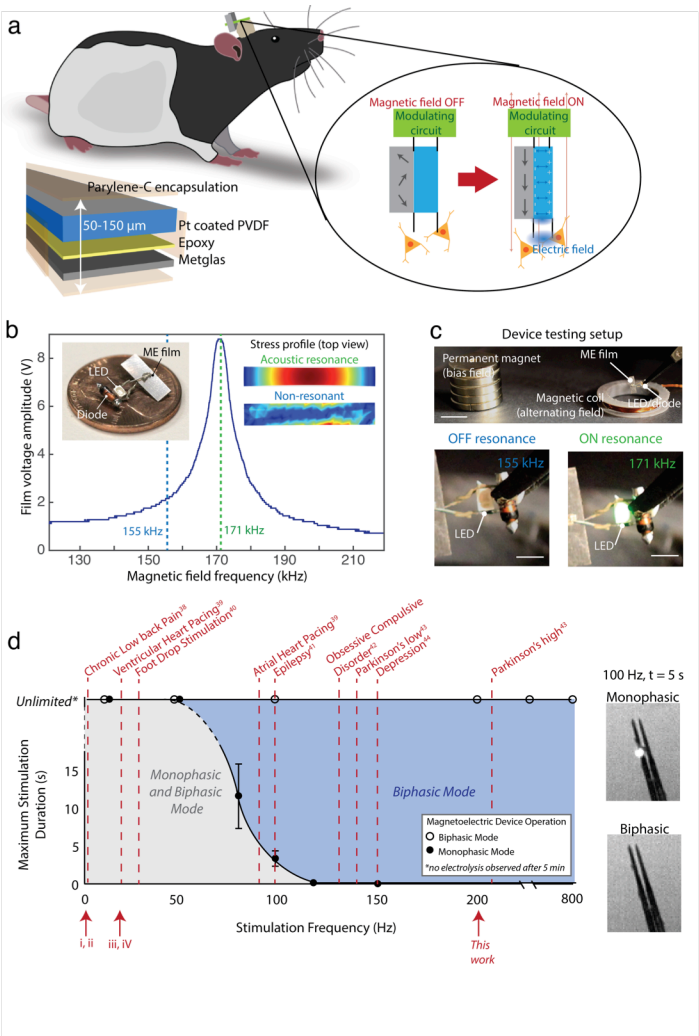

Figure 1 | ME films convert alternating magnetic fields into a voltage. (a) Diagram of a ME device on a freely moving rat for wireless neural stimulation. The active ME element consists of piezoelectric PVDF (blue) and Metglas (gray) laminate encapsulated by Parylene-C. Inset shows the operating principle whereby the strain produced when magnetizing the gray magnetostrictive layer is transferred to the blue piezoelectric layer, which creates a voltage across the film. (b) Example of a resonant response curve for a ME film showing that the maximum voltage is produced when the magnetic field frequency matches an acoustic resonance at 171 kHz. Photograph inset shows an example of an assembled ME stimulator. The "Stress profile" inset shows a top view of the stress produced in a ME film as calculated by a finite element simulation on and off resonance (COMSOL). (c) Device testing setup with a permanent magnet to apply a bias field and an electromagnetic coil to apply an alternating magnetic field (scale bars: upper = 1 cm, lower = 2 mm) (d) Maximum stimulation duration (using a 400 µs/phase pulse repeated at increasing frequencies) for a ME device in biphasic and monophasic operation. Maximum stimulation time is determined by time of electrolysis on a stereotrode in saline as evidenced by gas bubbles (error bars +/- 1 standard deviation for n=4 trials). Dashed lines indicate frequencies of electrical stimulation used in various clinical applications, showing that biphasic operation is necessary for many clinically relevant applications. Roman numerals indicate stimulation frequencies demonstrated by previously published miniature magnetic stimulators (i: Magnetothermal, Chen et. al, 2015, ii: Magnetothermal, Munshi et. al, 2017, iii: Mid-Field Optogenetics, Montgomery et. al, 2015, iv: RF Inductive Coupling, Freeman et. al, 2017).

We can further enhance the voltage generated by the ME films by applying a constant bias field with a permanent magnet or an electromagnet (Fig. 1c). Because the strain in the magnetostrictive material is a sigmoidal function of the magnetic field strength, the change in voltage produced by the alternating field is largest when the field oscillates about the midpoint of the sigmoid (Fig. S1)[28,29]. Thus, we use a bias field to offset the magnetic field near the center of the sigmoidal magnetostrictive response curve. This bias field allows us to generate therapeutic voltage levels while applying a small (few mT) alternating magnetic field using an electromagnetic coil and custom control circuitry that specifies the frequency and timing of the alternating magnetic field (Fig. S3).

To identify the operational frequencies for our ME stimulators we tested them in saline and found that with a biphasic stimulation waveform we could apply constant stimulation up to at least 800 Hz without significant hydrolysis. For this test we operated either one film for monophasic stimulation or two films for biphasic stimulation attached to a stereotrode (Microprobes) in saline (see Methods). We then measured the time at which we could see bubbles at the electrode tip resulting from hydrolysis. This hydrolysis event indicates conditions that would lesion the surrounding tissue. We found that with a monophasic stimulation waveform stimulation frequencies above 50 Hz produced hydrolysis while biphasic charge-balanced stimulation showed no hydrolysis up to the maximum tested frequency of 800 Hz. Compared to previously demonstrated miniature magnetic neural stimulators, the biphasic ME devices shown here are the first to access the high-frequency bands used for clinical applications like the treatment of Parkinson's disease and obsessive-compulsive disorder (Fig 1d).

An additional challenge for any wirelessly powered neural stimulator is to maintain a well-regulated stimulation voltage. This challenge is especially prevalent as devices become small, which often reduces the power transfer efficiency resulting in a greater sensitivity to the alignment between the device and power transmitter. ME materials offer two main advantages that can enable stable and effective stimulation even as devices become small and move with respect to the driver coils:

First, ME devices generate voltages well in excess of the effective stimulation potential, allowing them to be effective even if the materials are misaligned with the driver coils. At resonance, we have measured ME voltages in excess of 30 V at a field strength of only 1 mT (Fig. S2c, d). Because effective stimulation voltages are usually between 1-5 V, we can cap the applied voltage to this effective stimulation range using an LED or Zener diode. As long as the voltage generated by the ME film is greater than or equal to the capping voltage, we will apply approximately the same stimulus voltage regardless of the angle or distance between the driver coil and the ME film. For a typical film we found that we could reorient the film by +/- 80 degrees and maintain voltages in excess of 3 V (Fig. S1h). This large angular tolerance is aided by the large magnetic permeability of the Metglas layer, which

helps to direct the magnetic field lines along the long axis of the film, where they are most effective at creating a magnetostrictive response.

Second, the voltage generated by a piezoelectric material depends on the thickness of the piezoelectric layer and not the area of the film[30], allowing us to fabricate small magnetoelectric films that generate roughly the same stimulation voltage as larger devices. Figure S2 shows the peak voltage generated and quality factor for ME films of different areas. We found that, for a 52 μm thick PVDF layer, the voltage remains around 10 V even as the film length decreases. Variations of +/- 40 % in peak voltage and quality factors are likely due to defects produced during film fabrication, which may be reduced with improved manufacturing. We also verified that the output voltage depends only on the piezoelectric film thickness by measuring the peak voltages from ME devices with three different thicknesses of PVDF: 28 μm, 52 μm, and 110 μm. As expected, we see that the peak voltage increases linearly with the PVDF thickness and is independent of the film length. We calculated (and experimentally confirmed) that the power generated by a ME device is proportional to the film width for a given thickness and a length-to-width ratio >3 (see Fig. S2f). Despite the decrease in power as films become smaller, we calculate that films less than 1 cm long can generate up to 4 mW, which is more than sufficient for many wireless applications including neural stimulation[31].

Monophasic stimulation by ME films evoke action potentials *in vitro*

Using fluorescence microscopy to image voltage in cultured cells, we found that monophasic stimulation for 50 ms at 100 Hz by ME films reliably stimulated action potentials (APs). For these experiments we used “spiking” human embryonic kidney (HEK) cell lines that were modified to express sodium and potassium channels. These cells have spike-like electrical waveforms that are rectangular in shape and can last for a few seconds depending on the confluency of the culture[32]. To determine the relative timing between magnetic stimulation and action potential generation, we transfected these cells with ArcLight[33]-a genetically encoded voltage indicator that allows us to measure action potentials using fluorescence microscopy.

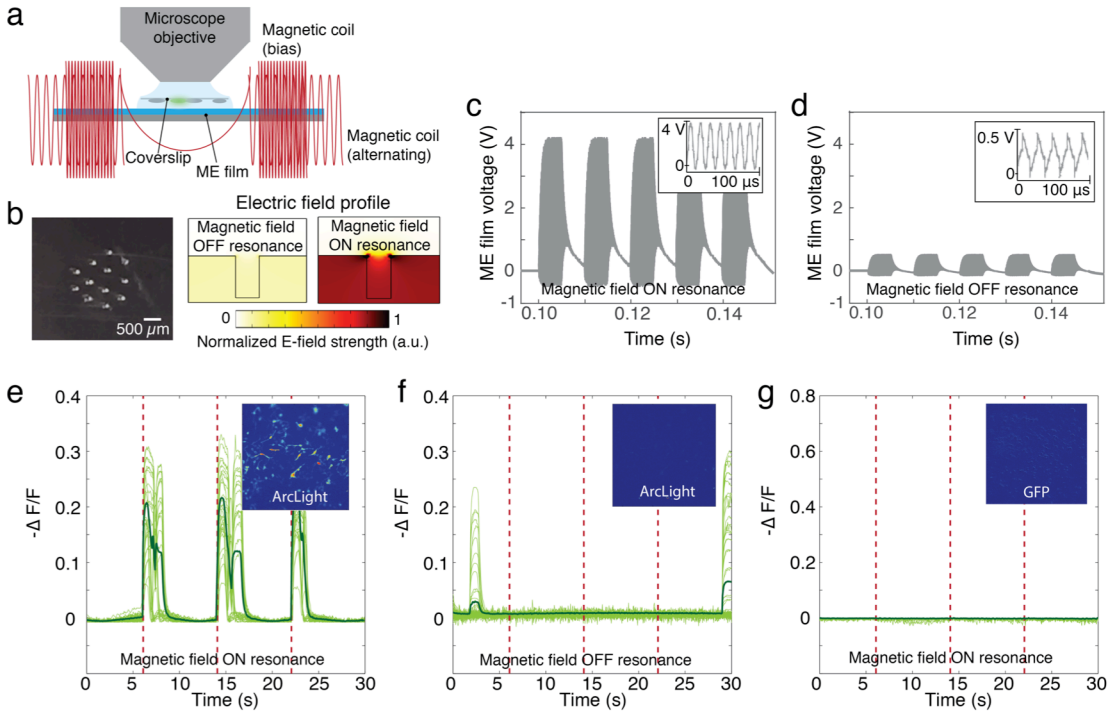

Figure 2 | Monophasic ME stimulators activate cells in vitro (a) Schematic of the experimental setup (b) Microscope image of holes stamped into the ME film and finite element simulation of the electric field shows that the holes produce fringing electric fields that overlap the culture cells (c) Voltage across the ME film when the magnetic field is on resonance and (d) off resonance. Insets show a zoom in of the high frequency carrier waveform. (e-g) Fluorescence from spiking HEKs transfected with ArcLight show action potentials are triggered by the ME film driven at resonance (e), but not when the film is driven off resonance (f). Fluorescence from HEK cells transfected with GFP show no response when the ME film is driven on resonance confirming that the measured ArcLight response is the result of a change in transmembrane potential and not an artifact of the magnetic field or acoustic resonance of the ME film.

To image fluorescence while we applied magnetic fields, we developed an experimental setup that allows us to place cells and ME films beneath an objective lens at the center of a 10 cm long solenoid with a 3 cm gap in the center. This configuration allowed us to place ME films, cells, and the objective lens at the center of the applied magnetic field (Fig. 2a). Two slightly larger coils placed on either side of the gap provide the constant bias field.

We then approximated an implanted ME stimulator using two experimental configurations: 1) growing cells directly on the ME film (Fig. S4) and 2) laying a coverslip with adherent cells on top of the ME film (Fig. 2). To culture cells directly on the ME film, we coated the top parylene layer with poly-l-lysine. The healthy proliferation of HEKs on the ME device indicates that this encapsulation approach prevents the ME materials from limiting cell growth (Fig. S4b). However, in a typical use case, the target cells may not adhere to the ME stimulator, so we also tested the response of cells laid on top of the ME materials. In this configuration we first grew the cells on coverslips for 3-5 days before inverting the coverslips and laying them on the ME for testing (Fig. 2, see Methods).

240
241 To create fringing electric fields that interact with the cultured cells, we stamped
242 holes in the ME film (Fig. 2b). The films were otherwise fabricated as described
243 above (Fig. 1, Methods). In experiments using ME films and Pt electrodes we found
244 that high-frequency biphasic stimulation at the ME resonance frequency (typically
245 20-150 kHz) was not effective to stimulate APs in cultured HEKs, as predicted by the
246 low-pass filtering properties of the cell membrane[9]. To create an effective
247 monophasic stimulus waveform, we used a Schottky diode to rectify the voltage to
248 create entirely positive or negative voltage waveforms depending on the diode
249 direction. This rectified waveform has a slowly varying monophasic envelope in the
250 <500 Hz frequency band where cells are responsive (Fig. 2c,d).
251
252 For both cells grown directly on the ME films and those placed in contact we found
253 that five stimulation pulses with an envelope frequency of 100 Hz consistently
254 stimulated APs in the spiking HEK cells (Fig. 2e, S4c, Supplementary Video 1).
255 Critically, this 10-500 Hz stimulation frequency is spans the therapeutic window for
256 many deep brain stimulation treatments[34], and difficult to achieve with other
257 wireless stimulators that compensate for low-efficacy energy harvesting by charging
258 on-board capacitors[35]. For our experiments, the carrier frequency of the magnetic
259 field was at the resonant frequency of the device, which varied between 20-40 KHz
260 depending on device length. To test stimulation reliability, we repeated the 5-pulse
261 stimulus three times over a period of 30 seconds. We observed APs for each
262 stimulation pulse in n = 43 cells on coverslips and n = 144 cells grown on films. We
263 confirmed that the APs stimulated by the ME film were in fact the result of resonant
264 excitation of the film and not an artifact of the applied magnetic fields by imaging
265 voltage-sensitive fluorescence when the magnetic field was tuned off of the resonant
266 frequency. For non-resonant excitation we observed no correlation between the
267 applied field and fluorescently detected APs in the spiking HEKs (Fig. 2f, S4d),
268 supporting the conclusion that APs were stimulated by the ME film at resonance. We
269 also confirmed that the fluorescent signal recorded indeed represents the voltage-
270 dependent ArcLight response by imaging cells transfected with voltage-independent
271 cytoplasmic GFP. These cells showed no change in fluorescence when the films were
272 driven at the resonant frequency (Fig. 2g).
273
274 **Biphasic stimulation by ME films evoke action potentials in brain slices**
275
276 As described above, biphasic stimulation is preferred for most applications due to
277 the desire to create a charge-balanced stimulus that reduces charge buildup and
278 undesired electrochemical reactions at the electrode surface[13]. While the voltage
279 waveform produced by ME films at resonance is biphasic, these resonant
280 frequencies (typically 20 – 150 kHz) are too high to produce reliable cell
281 stimulation, as described above. To create an effective biphasic stimulus in the
282 therapeutic window (100 – 200 Hz), we use two films with distinct resonant
283 frequencies connected to the same stimulating electrodes (Fig. 3a). The first film is
284 attached to a full wave rectifier, which is oriented to generate a positive pulse, while
285 the second film is attached to a full wave rectifier that generates a negative pulse.

286 The transistors block currents generated by one film from propagating through the
287 circuitry attached to the other film, ensuring that only one half of the circuit is active
288 at a time. By switching the magnetic field frequency between the two ME resonance
289 frequencies, we can alternate positive and negative phase stimulation to create a
290 biphasic neural stimulator (Fig. 3b-d). In this case the residual charge of -2.3 nC,
291 which discharges in <2 ms, implies that this stimulator can safely operate at
292 frequencies up to >500 Hz without accumulating charge.
293
294 We found that our biphasic ME stimulator is capable of repeatable neural
295 stimulation using neocortical brain slices derived from mice that express the
296 genetically encoded calcium indicator GCaMP3 in GABAergic neurons. To image
297 neural activity following ME stimulation we inserted a stereotrode attached
298 biphasic ME stimulator described above while we imaged GCaMP activity using
299 fluorescence microscopy (Fig. 3e-g, Methods). We chose neural stimulation
300 parameters similar to those commonly used for deep brain stimulation[34]: 100
301 biphasic pulses at 200 Hz with each phase lasting 175μs. When the magnetic field
302 was on we observed a corresponding increase in fluorescence in n=23 recordings in
303 neocortical layer 5 consistent with activity-mediated calcium increases
304 (Supplementary Video 2). Following bath application of tetrodotoxin (TTX , 500
305 nM) fluorescence increases were completely blocked in n=9 recordings confirming
306 that ME stimulation reliably evoked sodium-channel dependent action potentials in
307 nearby neurons.
308

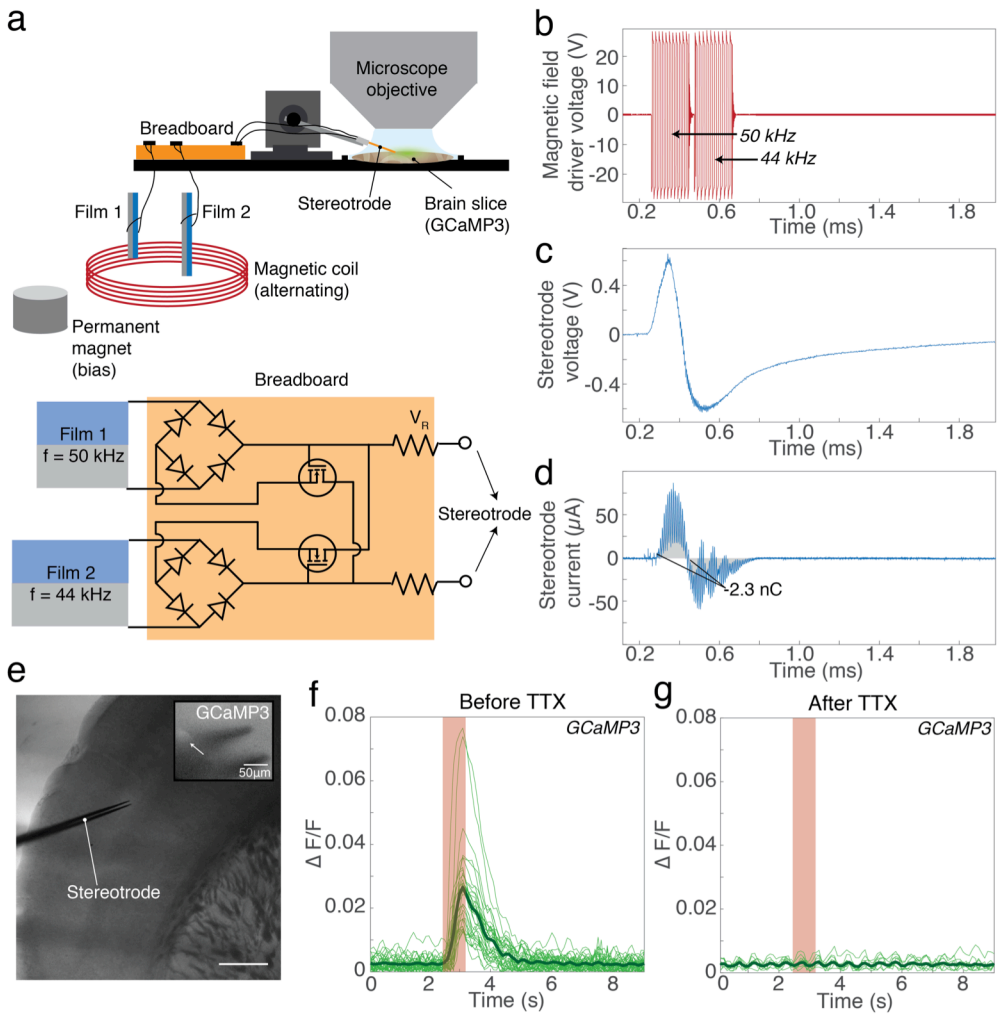

Figure 3 | Biphasic ME stimulators activate neurons in ex vivo brain slices (a) Schematic of experimental setup with two ME films for biphasic stimulation (b) Measured voltage waveform produced by our magnetic field generator. When coupled to the magnetic coils, this waveform produces magnetic fields that alternate between the resonant frequencies of the two ME films (c) Measured voltage across the stereotrode shows the expected biphasic pulse shape (d) Calculated current based on measuring the voltage across our load resistor (V_R) shows nearly perfect charge balancing with only 2.3 nC accumulating on the electrode per pulse train. (e) Bright field image of stereotrode in mouse cortex (scale bar = 1 mm) with inset of GCaMP signal averaged over a 600 μm x 600 μm region around stereotrode tip. Arrow indicating a fluorescing cell body near the stereotrode (f) Average GCaMP signal when resonant magnetic field is applied before (f) and after (g) adding TTX shows neural activity is induced by the ME stimulator. Thin green traces represent separate experiments from two different brain slices, and thick black traces represent the mean of all experiments.

309
310

311 **ME Neural Stimulation in Freely Moving Rats Shows Behavioral Efficacy**
312
313 A major advantage of our ME stimulators is the fact that remote activation enables
314 experiments with freely behaving animals. As a proof-of-principle we adapted our
315 biphasic stimulator for deep brain stimulation (DBS) in freely moving rats (Fig. 4).
316 To test ME stimulator efficacy, we used a previously reported protocol to test DBS in
317 hemi-parkinsonian rats[36]. In these experiments rats are injected with 6-OHDA in the
318 left medial forebrain bundle (MFB) to create a unilateral lesion of the substantia
319 nigra pars compacta (SNc). The animals are then placed in a 30 cm diameter circular
320 enclosure. Following a dose of methamphetamine, the hemi-parkinsonian rats have
321 been shown to rotate ipsilateral to the injection (e.g. left for injection into the left
322 MFB). During these rotations, the rat primarily moves using its contralateral (right)
323 forepaw, rarely placing the ipsilateral (left) forepaw onto the ground. When a
324 biphasic stimulus is applied at 200 Hz in the sub-thalamic nucleus (STN) using a
325 tethered electrode array stimulator, rats typically stop turning to the left and exhibit
326 more normal behavior such as moving with both forepaws, maintaining a steady
327 orientation, or turning to the contralateral side[34].
328
329 To create a wireless, biphasic ME stimulator for freely moving animals we added a
330 small permanent magnet to the ME stimulator to generate a bias field, and wrapped
331 the behavioral chamber with 18 AWG copper wire to create a solenoid (Fig. 4a, S5).
332 By integrating the small permanent magnet (< 0.25g) into the ME stimulator, we
333 could ensure that the bias field was constantly aligned with ME films as the animal
334 moved within the enclosure. We could also ensure that the positive and negative
335 stimuli had equal amplitudes by independently adjusting the distance between each
336 film and the permanent magnet. This ME stimulator was then connected to a
337 commercial electrode array (Microprobes) implanted in the STN (Fig 4b, see
338 Methods). We ensured that the stimulation voltage and current were within the safe
339 and therapeutic range by measuring the output of the ME stimulator connected to
340 an equivalent circuit model of the brain (Fig. 4c, see methods). Specifically, we
341 observed peak voltages of approximately +/-1.5 V and peak currents of
342 approximately +/- 100 μA for 400 us at approximately a 50% duty cycle (200 μs of
343 overall current per phase), which is within the effective stimulation range reported
344 for conventional wired stimulators[36]. When we tune the magnetic field frequency off
345 resonance we observe almost no generated voltage or current (Fig. 4c).

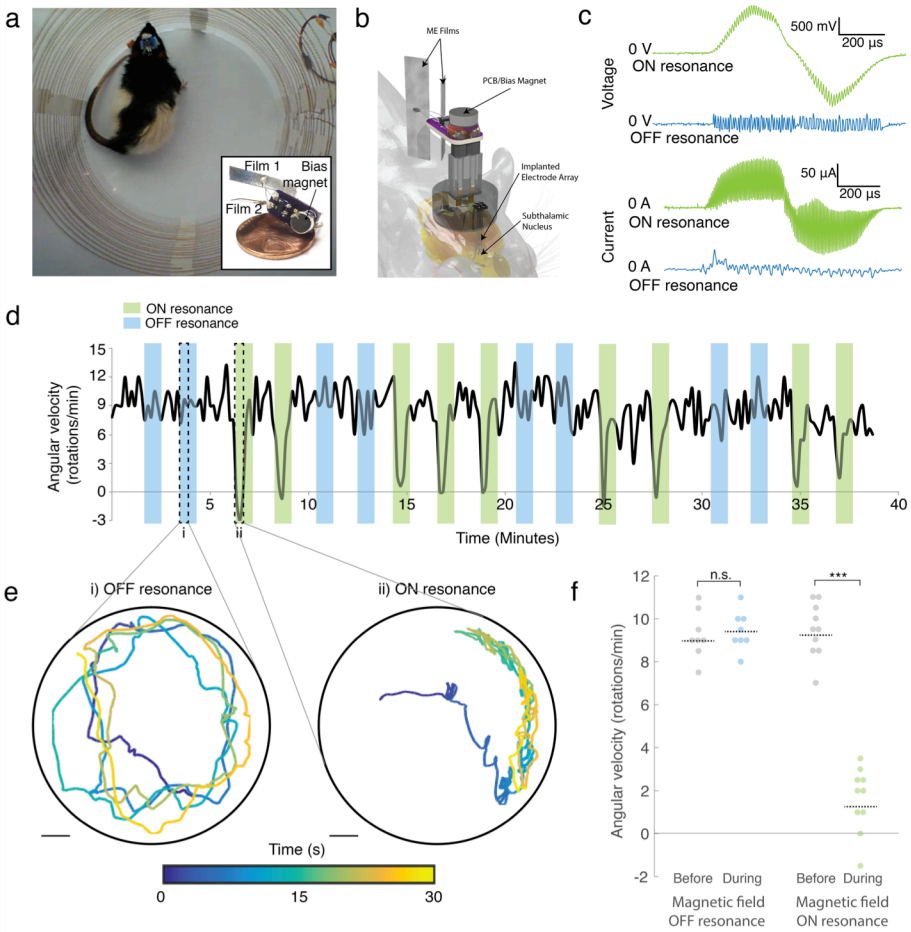

Figure 4 | Effective DBS in a freely moving rat using a wireless ME stimulator (a) Experimental setup showing rat in a circular enclosure wrapped with magnet wire. Inset shows a biphasic ME stimulator on a one cent coin (b) Schematic of the biphasic ME stimulator attached to the electrode array that is implanted into the STN (c) Measured voltage generated by the ME device and the current applied to the brain on resonance (green) and off resonance (blue). Approximately 100 µA biphasic stimulation is applied only when then the magnetic field frequency matches the resonance condition. (d) Angular velocity of the hemi-Parkinsonian rat over a 40 minute DBS trial with intervals of resonant and non-resonant stimulation shows that rotations are reduced only when the stimulator is activated by a resonant magnetic field (e) Typical trajectories show the location of the animal's head over two 30-second intervals denoted in c (scale bar = 5cm) (f) Average angular velocity of the rat during the 30 seconds before stimulation and the first 30 seconds of stimulation for each interval during the 40-min experiment shows a clear reduction in angular velocity only when the ME film is activated on resonance (*** P = 4×10^{-7}, n.s.=not significant P=0.70, paired t-test)

We then tested the wireless version of our biphasic ME stimulator mounted to the head of a freely behaving rat and found that ME stimulation showed efficacy comparable to previously reported wired DBS stimulators (Fig. 4). With a magnetic field applied at resonance, we found that one-minute periods of 200 Hz biphasic pulses resulted in a significant decrease in the animal's rotation rate (Fig. 4d green intervals). This decreased rotation was not observed when the magnetic stimulus frequency was tuned off resonance (Fig. 4d blue intervals). Plots of the head

trajectories show that the pathological rotations observed during off-resonant magnetic field stimulation are not present when the ME stimulator is active during resonant magnetic field stimulation (Fig. 4e, Methods). When averaged over all trials, average rotation rate during the first half of stimulation fell to a statistically significant 1.6 rotations per minute (rpm), compared to 9.3 rpm in the absence of stimulation, or 9.4 rpm during off-resonant stimulation (paired t-test, Fig. 4f). We further demonstrated the repeatability of this stimulator by repeating this stimulation protocol on a second rat and found similar results (Fig S5b).

With a weight of 0.67 g, the ME stimulators described here are the first reported miniature, magnetic, high frequency stimulator. Furthermore, by changing the frequency and timing of the external drive coils, we can generate a variety of stimulation patterns throughout the therapeutic window of 100-200 Hz with applications to other disease models. Additionally, calculations of the magnetic field strengths suggest that we can reconfigure the drive coils for a number of behavioral experiments by placing coils beneath the floor of an animal enclosure. Finite element simulations and measurements show that even at distance 4-5 cm above a drive coil, ME films generate sufficient voltage for stimulation (Fig. S6). This distance could be further improved by optimizing the geometry of the coils or increasing the power of the magnetic field.

Demonstration of multichannel deep brain stimulation in skull phantom using rice-sized ME films

In addition to supporting experiments in freely moving rodents, ME materials could enable miniaturized wireless stimulators that operate deep in the brain of large animals or human patients and are individually activated with an external electromagnet. To our knowledge, this is the first technology that enables independent external wireless control of multiple miniature stimulators deep beneath a human skull phantom. Figure 5a shows the predicted depth that various miniature antennas could be safely implanted under the skull and generate 1 mW of power, which is in the approximate maximum power required for high-frequency continuous neural stimulation[31]. As mentioned above, radio-frequency (RF) powered antennas that operate at frequencies above ~1 MHz have limitations in the amount of power that can safely be delivered to an implanted device without causing potentially harmful tissue heating. Simulations show that when operating with the safe power limits, RF-antennas must be placed on the surface of the brain or in very shallow regions to harvest 1 mW of power. "Mid-field" techniques[37], improve the RF coupling efficiency enabling deep operation, but because this approach operates at a fixed frequency there have yet to be demonstrations of individually addressable motes or biphasic stimulation. Other techniques for wireless power delivery discussed previously, such magnetic induction, also cannot achieve deep multichannel stimulation. For example, even using a higher operating frequency of 1 MHz an inductive coil with the same orientation and cross-sectional area as the ME films shown here would require a minimum of 500 turns of wire to generate 2 V using the same 0.5 mT field used here (assuming a typical Q-factor of

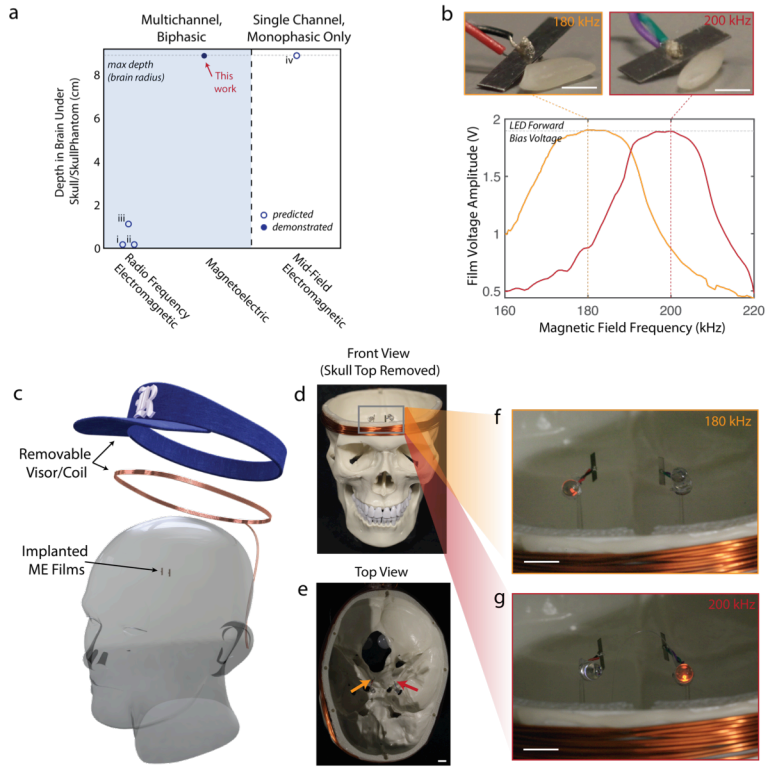

Figure 5 | Miniaturized Multichannel Stimulation in Human Skull Phantom (a) Comparison of effective depth beneath a human skull phantom for ME devices compared to other miniature wireless stimulators. Depth limit is based on safety limits to generate 1 mW. (i: Park et. al, *Proc Nat Ac Sci*, 2016 , ii:Yazdandoost et. al, *Asia Pac Microw Conf*, 2009, iii: Yazdandoost et. al, *Proc 37 Europ Microw Conf*, 2007, iv: Agrawal et. al, *Nat Biomed Eng*, 2017) (b) Photos of ME films next to a grain of rice and the corresponding voltage as a function of magnetic field frequency (field strength 1 mT, scale bars 2 mm) (c) Schematic of showing potential application of fully implanted ME films with the magnetic field generated by an external coil that can be incorporated into a hat or visor (d) Front view and (e) top view of skull phantom with the top removed to view LEDs (film locations indicated by arrows, scale bar 1 cm) (f) Photo of LEDs attached to ME films with the magnetic fields at applied at180 kHz and (g) 200 kHz. Selective illumination of the LEDs corresponding the resonant frequencies of the films demonstrates successful multichannel activation of individual films (scale bars 1 cm). Magnetic field strength was measured to be 0.5 mT at the location of the ME films.

10). Thus, devices based on magnetic inductors cannot be miniaturized without sacrificing available power as described previously[9].

As a proof-of-concept demonstration we show that two rice-sized ME films can be individually addressed at the center of a human skull phantom using an external electromagnet. These two-films with lengths of 8 mm and 10 mm have acoustic resonant frequencies of 180 and 200 kHz, which are determined by the film length. When these films are attached to an orange LED, their output voltage is capped at approximately 1.8 V, which helps to regulate the stimulation voltage and allows us to visualize film activation. ME films of this size are smaller than current DBS leads and could potentially be implanted into deep brain areas as shown in Fig 5c. Additionally, the magnetic stimulation coil is small enough to be incorporated into a stylish hat or visor that could be worn comfortably by a patient. When we placed

the two ME films at the center of a skull phantom we found that we could individually illuminate the LEDs on each film when we applied a magnetic field at the resonant frequency of the selected film (Fig 5d-g). For this experiment we used a 400 W power supply, which produced a field of approximately 0.5 mT at the center of the skull phantom. The top of the skull phantom was removed for visualization, but had no affect on our ability to drive the LED indicators. The number of stimulation channels could be increased with the addition of ME films with different resonant frequencies.

Outlook

To our knowledge, this is the first demonstration of a miniature, magnetic neural stimulator that 1) operates in the therapeutic band (100-200 Hz) in freely moving animals and 2) enables individually addressable miniature stimulators deep within a human skull phantom; however, the advantages of ME materials extend beyond these proof-of-principle demonstrations.

ME stimulators such as the one described in the in vivo rat experiment could have an immediate impact on the study of DBS therapies using rodent disease models. Because the ME stimulator is compatible with commercial implanted electrodes, and the magnetic stimulators can be adapted to a number of standard behavioral experiments or animal enclosures, our ME stimulators could readily replace the wired DBS stimulators currently in use. As a result, new experiments can be developed to probe the effects of chronic and continuous DBS or DBS in social contexts where wired DBS stimulators would be impracticable.

Additionally, ME materials have the potential to enable miniature neural stimulators that can be implanted deep in the brain of large animals or humans and addressed externally with a small electromagnet. As shown here, rice-sized films can be selectively activated based on unique resonant frequencies. Additional miniaturization is not expected to reduce the voltage produced by these films since the voltage depends on the thickness of the piezoelectric field and not the film length (Fig. S2 c), suggesting that even smaller films could serve as effective stimulators.

We also foresee applications for ME materials as a wireless power technology for more complex implantable bioelectronic devices. For example, the demonstrated ability of ME films to power LEDs implies that ME materials could power implantable optogenetic stimulators, or small integrated circuits for physiological monitoring.

To realize these fully implantable bioelectronic devices, work is needed to improve ME materials and fabrication processes to reliably produce high-quality miniature ME films, and encapsulate them for chronic use. For wearable technologies, it is also necessary to further miniaturize magnetic field generators so that they can be

458 battery powered and comfortably worn. These advances must also be accompanied
459 by in vivo testing to show safety and efficiency for chronic use.
460
461 Overall, ME materials have the potential to fill a key need for wireless power
462 delivery to miniature biphasic neural stimulators and other bioelectronic devices
463 where the major challenge is transferring energy over distances of several
464 centimeters without heating the tissue or suffering loss at interfaces between tissue,
465 bone, and air.
466
467 **References**

468 1. Hargreaves, D. G., Drew, S. J. & Eckersley, R. Kirschner Wire Pin Tract Infection
469 Rates: A randomized controlled trial between percutaneous and buried wires.
470 *J. Hand Surg. Br. Eur. Vol.* **29,** 374–376 (2004).

471 2. Roy, B., C., M. D. & A., T. P. The brain tissue response to implanted silicon
472 microelectrode arrays is increased when the device is tethered to the skull. *J.*
473 *Biomed. Mater. Res. Part A* **82A,** 169–178 (2007).

474 3. Markwardt, N. T., Stokol, J. & Rennaker, R. L. Sub-meninges implantation
475 reduces immune response to neural implants. *J. Neurosci. Methods* **214,** 119–
476 125 (2013).

477 4. Sahin, M. & Pikov, V. Wireless Microstimulators for Neural Prosthetics. *Crit.*
478 *Rev. Biomed. Eng.* **39,** 63–77 (2011).

479 5. Pinnell, R. C., Vasconcelos, A. P. De & Cassel, J. C. A Miniaturized ,
480 Programmable Deep-Brain Stimulator for Group-Housing and Water Maze
481 Use. *Front. Neurosci.* **12,** 1–11 (2018).

482 6. Nurmikko, A. V. Approaches to large scale neural recording by chronic
483 implants for mobile BCIs. in *2018 6th International Conference on Brain-*
484 *Computer Interface (BCI)* 1–2 (2018). doi:10.1109/IWW-BCI.2018.8311503

485 7. International, I. & Safety, E. *IEEE Standard for Safety Levels with Respect to*
486 *Human Exposure to Radio Frequency Electromagnetic Fields , 3 kHz to 300 GHz*.
487 **2005,** (2006).

488 8. Fotopoulou, K. & Flynn, B. W. Wireless Power Transfer in Loosely Coupled
489 Links : Coil Misalignment Model. *IEEE Trans. Magn.* **47,** 416–430 (2011).

490 9. Freeman, D. K. *et al.* A sub-millimeter, inductively powered neural stimulator.
491 *Front. Neurosci.* **11,** 1–12 (2017).

492 10. De Hemptinne, C. *et al.* Therapeutic deep brain stimulation reduces cortical

493 phase-amplitude coupling in Parkinson's disease. *Nat. Neurosci.* **18,** 779–786
494 (2015).

495 11. Alonso, P. *et al.* Deep brain stimulation for obsessive-compulsive disorder: A
496 meta-analysis of treatment outcome and predictors of response. *PLoS One* **10,**
497 1–16 (2015).

498 12. Theodore, W. H. & Fisher, R. S. Review Brain stimulation for epilepsy. *Lancet*
499 **3,** 111–118 (2004).

500 13. Merrill, D. R., Bikson, M. & Jefferys, J. G. R. Electrical stimulation of excitable
501 tissue: Design of efficacious and safe protocols. *J. Neurosci. Methods* **141,** 171–
502 198 (2005).

503 14. Parastarfeizabadi, M. & Kouzani, A. Z. Advances in closed-loop deep brain
504 stimulation devices. *J. Neuroeng. Rehabil.* **14,** 79 (2017).

505 15. Montgomery, K. L. *et al.* Wirelessly powered, fully internal optogenetics for
506 brain, spinal and peripheral circuits in mice. *Nat. Methods* **12,** 969–974
507 (2015).

508 16. Ho, J. S. *et al.* Self-Tracking Energy Transfer for Neural Stimulation in
509 Untethered Mice. *Phys. Rev. Appl.* **24001,** 1–6 (2015).

510 17. Carrey, J. *et al.* Simple models for dynamic hysteresis loop calculations of
511 magnetic single-domain Simple models for dynamic hysteresis loop
512 calculations of magnetic single-domain nanoparticles : Application to
513 magnetic hyperthermia optimization. *J. Appl. Phys.* **83921,** (2015).

514 18. Chen, R., Romero, G., Christiansen, M. G., Mohr, A. & Anikeeva, P. Wireless
515 magnetothermal deep brain stimulation. *Science* **347,** 1477–80 (2015).

516 19. Munshi, R. *et al.* Magnetothermal genetic deep brain stimulation of motor
517 behaviors in awake, freely moving mice. *Elife* **6,** 1–26 (2017).

518 20. Johnson, B. C. *et al.* StimDust : A 6.5mm^3 , Wireless Ultrasonic Peripheral
519 Nerve Stimulator with 82 % Peak Chip Efficiency. *2018 IEEE Cust. Integr.*
520 *Circuits Conf.* (2018).

521 21. Seo, D. *et al.* Wireless Recording in the Peripheral Nervous System with
522 Ultrasonic Neural Dust. *Neuron* **91,** 529–539 (2016).

523 22. Piech, D. K. *et al.* StimDust: A 2.2 mm3, precision wireless neural stimulator
524 with ultrasonic power and communication. 1–35

525 23. Nan, T. *et al.* Acoustically actuated ultra-compact NEMS magnetoelectric

526 antennas. *Nat. Commun.* **8,** 1–7 (2017).

527 24. O'Handley, R. C., Huang, J. K., Bono, D. C. & Simon, J. Improved Wireless,
528 Transcutaneous Power Transmission for *In Vivo* Applications. *IEEE Sens. J.* **8,**
529 57–62 (2008).

530 25. Yue, K. *et al.* Magneto-Electric Nano-Particles for Non-Invasive Brain
531 Stimulation. *PLoS One* **7,** 1–5 (2012).

532 26. Guduru, R. *et al.* Magnetoelectric 'spin' on stimulating the brain. *Nanomedicine*
533 **10,** 2051–2061 (2015).

534 27. Ribeiro, C., Correia, V., Martins, P., Gama, F. M. & Lanceros-Mendez, S. Proving
535 the suitability of magnetoelectric stimuli for tissue engineering applications.
536 *Colloids Surfaces B Biointerfaces* **140,** 430–436 (2016).

537 28. Zhai, J., Dong, S., Xing, Z., Li, J. & Viehland, D. Giant magnetoelectric effect in
538 Metglas/polyvinylidene-fluoride laminates. *Appl. Phys. Lett.* **89,** 8–11 (2006).

539 29. Kulkarni, a. *et al.* Giant magnetoelectric effect at low frequencies in polymer-
540 based thin film composites. *Appl. Phys. Lett.* **104,** 0–5 (2014).

541 30. Wan, C. & Bowen, C. R. Multiscale-structuring of polyvinylidene fluoride for
542 energy harvesting: the impact of molecular-, micro- and macro-structure. *J.*
543 *Mater. Chem. A* **5,** 3091–3128 (2017).

544 31. Amar, A. Ben, Kouki, A. B. & Cao, H. Power approaches for implantable medical
545 devices. *Sensors (Switzerland)* **15,** 28889–28914 (2015).

546 32. Park, J. *et al.* Screening fluorescent voltage indicators with spontaneously
547 spiking HEK cells. *PLoS One* **8,** 1–10 (2013).

548 33. Jin, L. *et al.* Single Action Potentials and Subthreshold Electrical Events
549 Imaged in Neurons with a Fluorescent Protein Voltage Probe. *Neuron* **75,**
550 779–785 (2012).

551 34. So, R. Q., Mcconnell, G. C. & Grill, W. M. Frequency-dependent , transient
552 effects of subthalamic nucleus deep brain stimulation on methamphetamine-
553 induced circling and neuronal activity in the hemiparkinsonian rat. *Behav.*
554 *Brain Res.* **320,** 119–127 (2017).

555 35. Sun, Y. *et al.* Wirelessly Powered Implantable Pacemaker with On - Chip
556 Antenna. *IEEE* 1242–1244 (2017).

557 36. Summerson, S. R., Aazhang, B. & Kemere, C. T. Characterizing Motor and
558 Cognitive Effects Associated With Deep Brain Stimulation in the GPi of Hemi-

559 Parkinsonian Rats. *IEEE Trans. Neural Syst. Rehabil. Eng.* **22,** 1218–1227
560 (2014).

561 37. Agrawal, D. R. *et al.* Conformal phased surfaces for wireless powering of
562 bioelectronic microdevices. *Nat. Biomed. Eng.* **1,** 1–16 (2017).

563 38. Schabrun, S. M., Jones, E., Elgueta Cancino, E. L. & Hodges, P. W. Targeting
564 chronic recurrent low back pain from the top-down and the bottom-up: a
565 combined transcranial direct current stimulation and peripheral electrical
566 stimulation intervention. *Brain Stimul* **7,** 451–459 (2014).

567 39. Mulpuru, S., Madhavan, M., McLeod, C., Cha, Y.-M. & Friedman, P. Cardiac
568 Pacemakers : Function , Troubleshooting , and Management. *J. Am. Coll.*
569 *Cardiol.* **69,** (2017).

570 40. Kesar, T. M. *et al.* Novel Patterns of Functional Electrical Stimulation Have an
571 Immediate Effect on Dorsiflexor Muscle Function During Gait for People
572 Poststroke. *Phys. Ther.* **90,** 55–66 (2010).

573 41. Bewernick, B. H. *et al.* Nucleus Accumbens Deep Brain Stimulation Decreases
574 Ratings of Depression and Anxiety in Treatment-Resistant Depression. *Biol.*
575 *Psychiatry* **67,** 110–116 (2010).

576 42. Park, S. Il *et al.* Stretchable multichannel antennas in soft wireless
577 optoelectronic implants for optogenetics. *Proc. Natl. Acad. Sci.* **113,** E8169–
578 E8177 (2016).

579 43. Yazdandoost, K. Y. A 2.4 GHz antenna for medical implanted communications.
580 *APMC 2009 - Asia Pacific Microw. Conf. 2009* 1775–1778 (2009).
581 doi:10.1109/APMC.2009.5384240

582 44. Yazdandoost, K. Y. & Kohno, R. An antenna for medical implant
583 communications system. *Proc. 37th Eur. Microw. Conf. EUMC* 968–971 (2007).
584 doi:10.1109/EUMC.2007.4405356

585

586

Methods

General Statistical Methods

Error bars in Figure S2fgdenote +/- one standard deviation for n=~50 data points. We furthermore performed a Tukey's Honest Significant Difference test on the data in Figure S2g, which indicated that the voltage produced at each different PVDF thickness is significantly different. Paired t-tests were used for the rotation tests in figure 4e.

Film Fabrication

To fabricate ME films, we used Metglas SA1 alloy (Metglas Inc) for the magnetostrictive layer and polyvinylidenefluoride "PVDF" (precision acoustics) for the piezoelectric layer. The PVDF films used for these experiments were pre-stretched and poled by the manufacturer. The two layers were bonded together using an epoxy capable of transferring the mechanical stress between the two layers (Hardman double bubble red epoxy). Prior to bonding the two layers together, we sputtered a thin layer of platinum (<100 nm) as a top electrode on the PVDF. Both the Metglas and PVDF were plasma cleaned using O_2 plasma for five minutes before epoxying. After the epoxy set, the films were cut into the desired rectangular shape using scissors, taking care to cut the long axis of the film along the stretching direction of the PVDF. We then attached wires using conductive epoxy to either side of the films in order to measure the electrical capabilities of the film. We found that attaching wires in the center dramatically increased the resonant voltage. However for convenience, the wires were attached near the ends of the films during the in vitro experiments. In many cases we also attached additional electronic components such as diodes or LEDs to the wires attached to the films as noted in the appropriate sections in the main text. Finally the devices were coated in 5-10 μm of parylene-C (Labcoater 2). Initially this coating was used to electrically insulate and protect the devices during in vitro experiments, but we also found that the encapsulation increases the resonant voltage, which could be due to increased mechanical coupling from the encapsulation.

Bench Top Electrolysis Tests

The stimulator shown in Fig 4a was wired to a stereotrode immersed in saline under a microscope in order to observe the formation of bubbles from electrolysis at the tips. During monophasic stimulation we used only one resonant frequency and during biphasic stimulation we used two frequencies as demonstrated above. In each case the pulse time was a 400 μs/phase. We determined the limit of stimulation time as when the first bubble began to appear at the tips of the electrode and repeated each data point 4 times.

Magnetic Field Generation (Fig. S3)

Each magnetic field generator consists of two major components, 1) Magnetic coils used for the alternating magnetic field (described in the main text and optimized for each experiment) and 2) Electronic drivers to control voltage and timing of the alternating current in the coils (the same for all experiments).

633
634 To maintain simplicity, efficiency, and low cost the coils were driven with full H-
635 Bridge style switching circuits. The drivers are designed to deliver high currents to
636 the drive coils in the form of bi-phasic pulse trains. This reduces the cost and
637 complexity of the driver itself, as well as the power supply and control circuitry
638 when compared to arbitrary function generators. The design also has potential for
639 improved operational efficiency through impedance matching with the drive coils.
640 Furthermore, it is also possible to regulate power delivered to the drive coils on the
641 fly by adjusting the duty cycle of the current pulses, allowing power being delivered
642 to the ME film to be easily controlled digitally while maintaining the resonant
643 carrier frequency. The output carrier and pulse frequencies of the magnetic field are
644 generated using a TeensyLC board and custom Arduino code to generate the specific
645 pulse timings to deliver controlled ME stimulation (Fig. S3c,d).
646
647 These coils and drivers can be combined in different ways to generate the
648 appropriate field for a given experiment. For example, the setup used to generate
649 the alternating field in the in vivo rotation experiments consisted of four sets of coils
650 each with five turns powered by one driver with all four drivers synced to the same
651 output signal. In this way we can generate sufficient power to generate a mT-scale
652 magnetic fields over the whole behavioral area (Fig. S5a).
653
654 Cell Culture
655 For experiments performed on coverslips, HEK cells expressing sodium channel
656 $Na_{1.3}$ and potassium channel $K_{2.1}$ were grown on 12 mm poly-l-lysine coated
657 coverslips to approximately 30% confluency. The cells were then transfected with
658 the genetically encoded voltage indicator ArcLight using Lipofectamine (Invitrogen)
659 following manufacturer's recommendations. Two to three days after transfection
660 the coverslips were inverted onto ME films for testing. Preparation of GFP controls
661 followed the same procedure with the exception of replacing the ArcLight vector
662 (AddGene) with a GFP expression vector (AddGene). For experiments performed
663 with cells grown on the films, HEK cells transfected with ArcLight were placed onto
664 parylene coated poly-l-lysine treated films. The films were placed in cellular media
665 overnight and tested the following day.
666
667 ArcLight and GFP were excited at 460 nm with an LED light source. Fluorescence
668 images were collected at 33 fps using a CCD camera. Images were analyzed using
669 Matlab to quantify fluorescence changes in individual cells. In vitro testing was
670 performed in extracellular buffer (ECB, in mM: NaCl 119, KCl 5, Hepes 10, $CaCl_2$ 2,
671 $MgCl_2$ 1; pH 7.2; 320mOsm)
672
673 Figure S4b was obtained by growing unmodified HEK cells on a film submerged in
674 cellular media for five days. The cells were then stained with Hoechst and Calcein-
675 AM to label the nucleus and membrane respectively in living cells. The cells were
676 then fixed and imaged using a confocal microscope.
677
678

679 Mouse Brain Slice Procedures
680 We used 40 day old GAD2-GCaMP3 mice, generated by crossing GAD2-Cre (JAX #
681 10802) with flox-GCaMP3 (JAX # 14538) animals. Preparation of brain slices
682 followed procedures described by Ting et al.[45] and was carried out in accordance
683 with National Institutes of Health guidelines and approved by the UTHealth animal
684 welfare committee. Mice were deeply anesthetized with Isoflurane and perfused
685 with ice cold NMDG-based solution consisting of (in mM): 92 NMDG, 2.5 KCl, 1.25
686 NaH_2PO_4, 10 $MgSO_4$, 0.5 $CaCl_2$, 30 $NaHCO_3$, 20 glucose, 20 HEPES, 2 thiouera, 5 Na-
687 Ascorbate, 3 Na-pyruvate, saturated with 95% O_2 and 5% CO_2., at a rate of ~6
688 ml/min. Coronal brain slices (300 μm) were cut using a vibratome (Leica VT1200S),
689 incubated for 15 min at 35 °C in NMDG solution, and then transferred to a chamber
690 held at room temperature containing (in mM): 92 NaCl, 2.5 KCl, 1.25 NaH_2PO_4, 2
691 $MgSO_4$, 2 $CaCl_2$, 30 $NaHCO_3$, 25 glucose, 20 HEPES, 2 thiouera, 5 Na-Ascorbate, 3 Na-
692 pyruvate, saturated with 95% O_2 and 5% CO_2. For experiments, slices were placed
693 into a recording chamber perfused with ACSF containing (in mM): 126 NaCl, 2.5 KCl,
694 1.25 NaH_2PO_4, 2 $MgCl_2$, 2 $CaCl_2$, 26 $NaHCO_3$, 10 glucose), held at 32-34 °C using an
695 inline heater. NBQX (10 μM) was included in the bath solution to block AMPA
696 receptor-mediated synaptic transmission. The stereotrode was placed in layer 5 of
697 somatosensory (barrel) cortex.
698
699 GCaMP3 was excited at 460 nm with an LED light source. Fluorescence images were
700 collected at 9.8 fps using a CCD camera attached to an Olympus BX51WI microscope.
701 Images were analyzed using Matlab to quantify fluorescence changes in 600 x 600
702 μm regions around the stereotrode tips.
703
704
705 Implant Design and Rat Surgical Procedures
706
707 Two male Long-Evans rats (n ≈ 1, 400 g) were anesthetized with isoflurane gas. Five
708 percent isoflurane was used to induce anesthesia and two percent was used to
709 maintain anesthetic depth. Buprenorphine (0.04 mg/kg) was administered 30
710 minutes prior to ear bars for analgesia. 5 - 7 skull screws were placed to anchor the
711 electrode array. Skull screws were bound to skull with Metabond dental acrylic. A
712 craniotomy was made to accommodate the micro electrode array and expose an
713 injection site for neurotoxin. A 30 gauge needle bent at the tip cut and pulled away
714 the dura mater covering of the brain. Desipramine (DMI) reconstituted in saline at a
715 concentration of 15 mg/mL was injected IP to protect noradrenergnic neurons. The
716 dose of DMI was approximately 15 mg/kg and injected approximately 30 minutes
717 prior to administration of neurotoxin. To induce a hemiparkinsonian lesion, 8 ug of
718 6-hydroxydopamine (OHDA) at 2 ug/uL in saline was injected at 0.2 uL/min into the
719 mid forebrain bundle (MFB -1.2 ML, -4 AP, and -8.1 DV). STN stimulation was
720 delivered via a 2x2 platinum iridium microelectrode array (Microprobes) with 600 x
721 600 μm spacing of 75 μm electrodes. Each electrode had a nominal 10 kOhm
722 impedance. The electrode array was lowered to -2.6 ML, -3.6 AP, and approximately
723 -8.2 DV from bregma. The array was fixed to the skull with dental acrylic. All

experiments were approved by the Institutional Animal Care and Use Committee of Rice University.

Prior to stimulating each rat with the magnetoelectric stimulator, the stimulator power was estimated via a benchtop approximation of the rodent electrode impedance. Constant current stimulation of the rodent brain with an A-M Systems 4100 stimulator produced characteristic voltage waveforms that approximated a simplified parallel RC circuit. A 56 kOhm resistor, and 440 pF capacitor in parallel closely approximated the impedance characteristics of the rat brain across the stimulating electrodes. Using this circuit model, we estimated the field strengths and pulse durations necessary to produce the desired stimulation effects and confirm that the stimulation was charge balanced prior to rodent experimentation.

Rotation Test Experiments

Prior to performing the rotation tests the rat was briefly anesthetized with 5% isoflurane gas and injected intraperitoneally (IP) with methamphetamine (0.31 ml 1.25 mg/kg) and the wireless biphasic stimulator was plugged into the implanted electrode array. After the anesthesia had worn off (about 5-10 min) the rat was placed in the cylindrical behavioral chamber. The magnetic field was applied over the whole behavioral area to the films on the device (Fig S5a).

The magnetic field was applied on resonance and off resonance for one minute at various times during the 40-minute trial. The resonant frequencies were 73 kHz and 77 kHz and the off resonant frequencies were 63 kHz and 87 kHz.

Rodent Tracking

Head position on the rotation task was generated using a slightly modified version of DeepLabCut[46] to track ears, snout, and implant. A dataset totaling 286 frames from both the on and off resonance rotation tasks was hand labeled and trained for approximately 140,000 iterations.

Skull Phantom Demonstration

At the magnetic field frequencies used for this experiment bone and tissue are effectively transparent[47], so we selected a life sized skull with the size of an average human adult head as a phantom (Orient Infinity Limited). It was wrapped with 18 AWG magnet wire as shown in Fig 5. The coil consisted of four coils in parallel each wired to an individual magnetic field driver. All drivers were wired to the same input frequency signal and powered from the same power supply. The films were suspended at the center of the skull phantom. Orange LEDs (Chanzon) with a diode antiparallel were attached to the films for wireless verification of the voltage generated by the films. For visualization purposes the skull top was removed to better photograph the LED.

References

45. Ting, J. T., Daigle, T. L., Chen, Q. & Feng, G. Acute brain slice methods for adult and aging animals: application of targeted patch clampanalysis and optogenetics. *Methods Mol. Biol.* **1183,** 221–242 (2014).

46. Mathis, A. *et al.* Markerless tracking of user-defined features with deep learning. *arXiv [cs.CV]* 1–14 (2018).

47. Bottomley, P. A. & Andrew, E. R. RF magnetic field penetration, phase shift and power dissipation in biological tissue: Implications for NMR imaging. *Phys. Med. Biol.* **23,** 630–643 (1978).

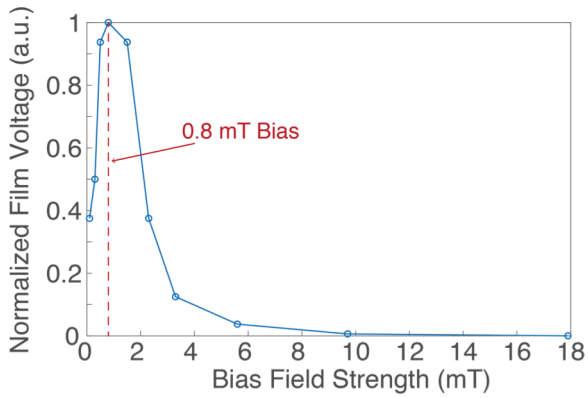

Supplemental Figure 1 | Film output voltage as a function of bias field The peak resonance voltage is significantly increased by a modest bias field that can be produced by a permanent magnet.

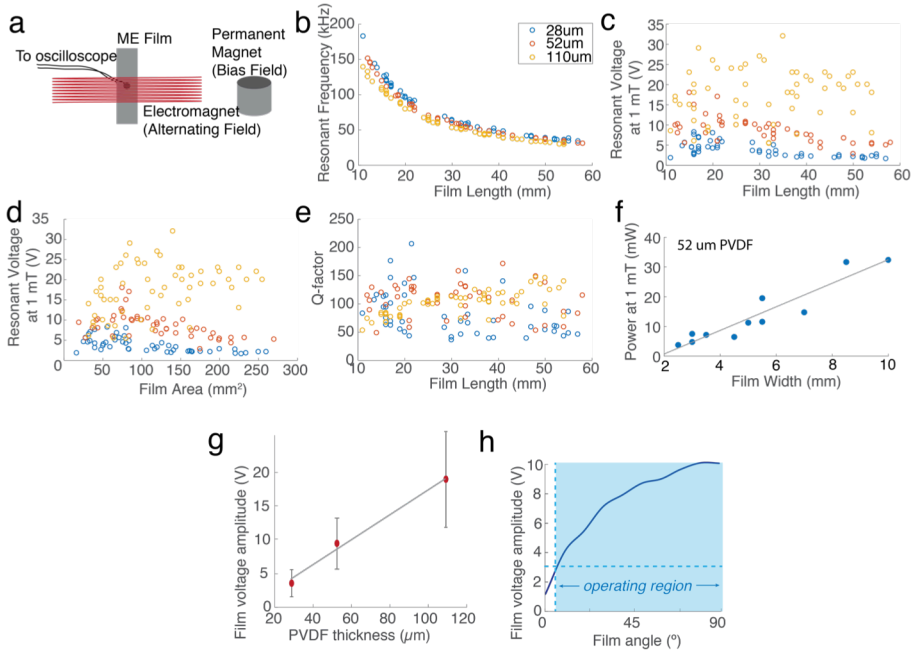

Supplemental Figure 2 | ME properties as a function of film size (a) Schematic of experimental setup used to gather data. Testing was performed for ME films with three different PVDF thicknesses: 28 (blue), 52 (red), and 110 (yellow) μ m (b) Resonant frequency as a function of film length (c) Output voltage as a function of film length (d) Output voltage as a function of film surface area (e) Q-factor as a function of film length (f) Maximum power output as a function of film width for 52um PVDF thickness (g) Peak resonant voltage plotted vs. PVDF thickness shows that the peak ME voltage increases with the PVDF thickness. Error bars indicate +/- 1 standard deviation for n ≈ 50 films for each thickness. (h)ME voltage as a function of angle between the film and the coil. Blue region shows the range of operating angles for which the voltage is greater than the expected stimulation voltage

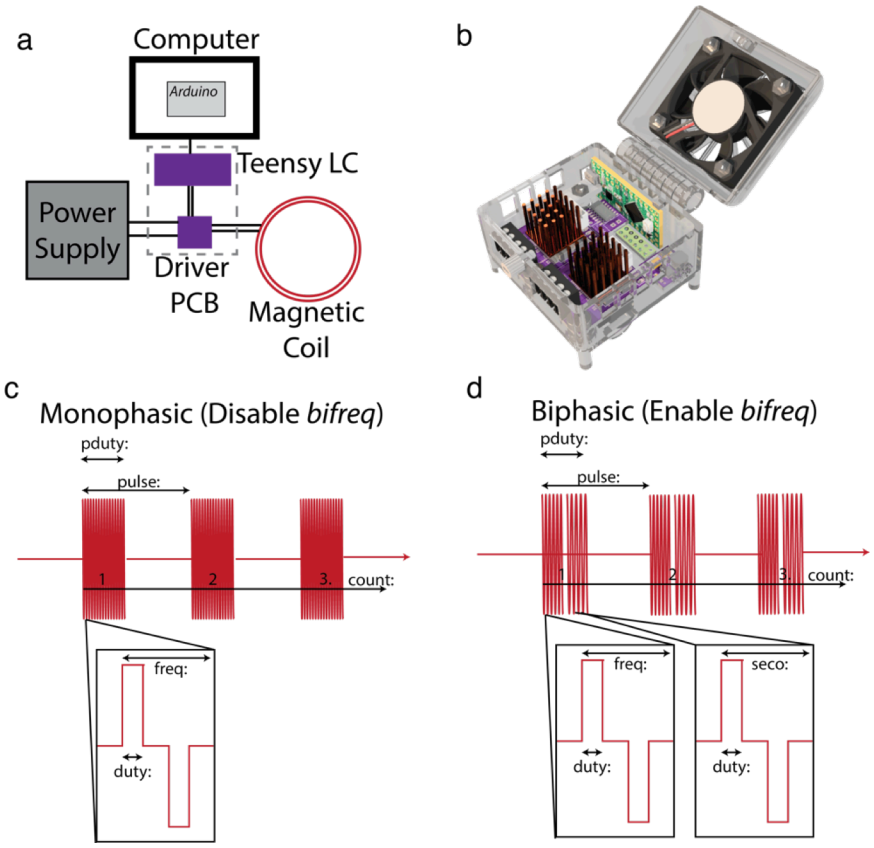

Supplemental Figure 3 | Magnetic Field Driver (a) Schematic of the major components of the magnetic field driver. Dashed line denotes components rendered in (b). (c) Output waveform for monophasic stimulation and the parameters that can be controlled by the drive software (d) Output waveform for biphasic stimulation, and the parameters that can be controlled by the driver software.

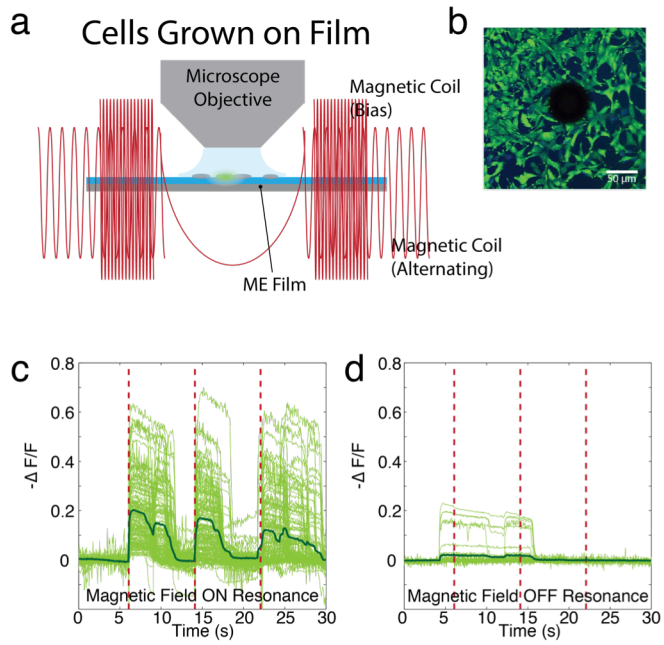

Supplemental Figure 4 | ME stimulation of cells grown directly on ME film (a) Schematic of experimental setup (b) Microscope image of fixed cells adherent to the region around a stamped hole (Hoechst/Calcein-AM, cells labeled prior to fixing) (c) ArcLight fluorescence of spiking HEK cells when magnetic field is on resonance and (d) off resonance.

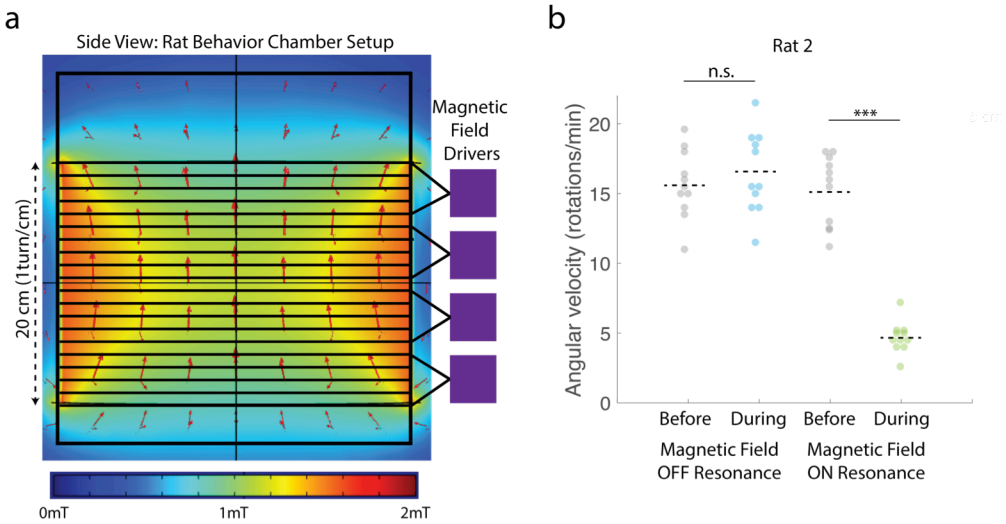

Supplemental Figure 5 | Magnetic Field for DBS Rotation Experiment (a) Schematic shows the location and spacing of wires and the number of drivers used to generate the alternating magnetic field overlaying a COMSOL simulation of magnetic field strength in the chamber (b) Results from rotation test in Rat 2: Angular velocity in the 30 seconds before stimulation and the first 30 seconds of stimulation shows a clear reduction in angular velocity only when the ME film is activated on resonance (*** $P = 1.5 \times 10^{-8}$, n.s.=not significant P=0.27, paired t-test)

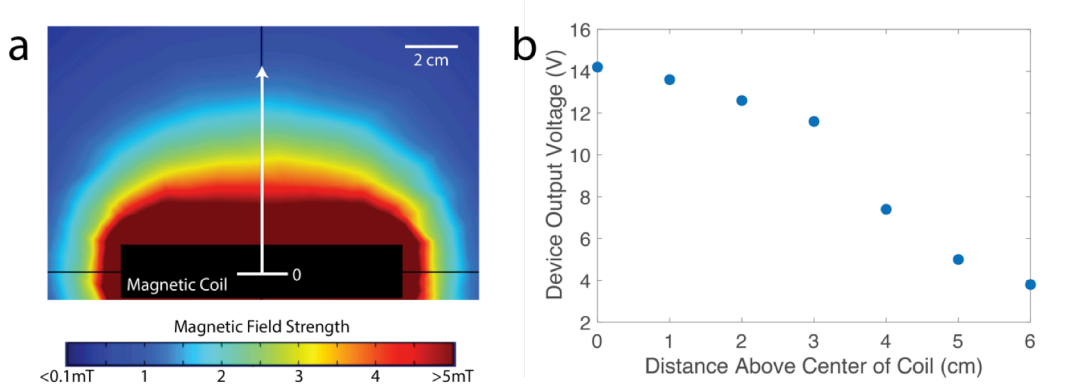

Supplemental Figure 6 | ME devices operate several centimeters above a single magnetic coil
(a) COMSOL simulation of magnetic field above a circular coil and (b) Measured device output voltage as a function of distance above the coil